Supplementary Information

All-in-One Structured Textile Energy Storage Electrodes Prepared via Janus Bond Assembly-Induced Electrodeposition

Seokmin Lee[a], Younji Ko[a], Woojae Chang[a], Cheong Hoon Kwon[b], Younghoon Kim[c,], Bongjun Yeom[d,]*, Jinhan Cho[a,e,]**

[a] Department of Chemical and Biological Engineering, Korea University, Seoul 02841, Republic of Korea.

[b] Division of Energy Engineering, Kangwon National University, Samcheok, 25913, Republic of Korea

[c] Department of Chemistry, Kookmin University, Seoul 02707, Republic of Korea.

[d] Department of Chemical Engineering, Hanyang University Seoul 04763, Republic of Korea.

[e] KU-KIST Graduate School of Converging Science and Technology, Korea University, Seoul 02841, Republic of Korea.

*Corresponding authors.

E-mail addresses: younghoon.kim@kookmin.ac.kr (Y. Kim), byeom@hanyang.ac.kr (B. Yeom), jinhan71@korea.ac.kr (J. Cho)

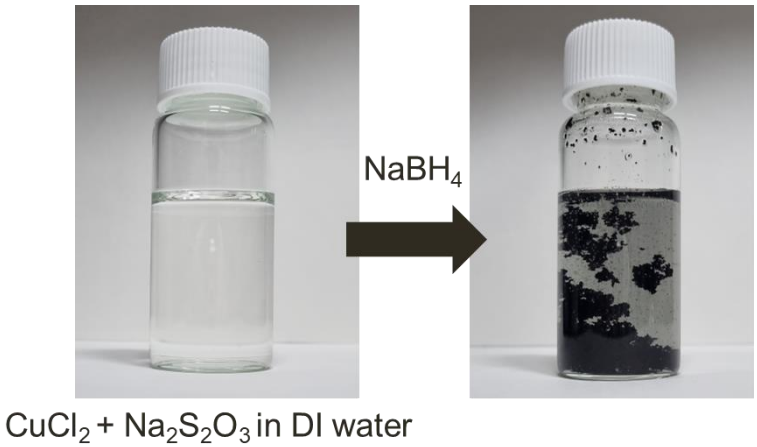

Fig. S1. Preparation the of Cu_xS NPs using sodium thiosulfate ($Na_2S_2O_3$) and reducing agent ($NaBH_4$) in only aqueous phase. The formed Cu_xS NPs were aggregated showing the poor dispersion in water.

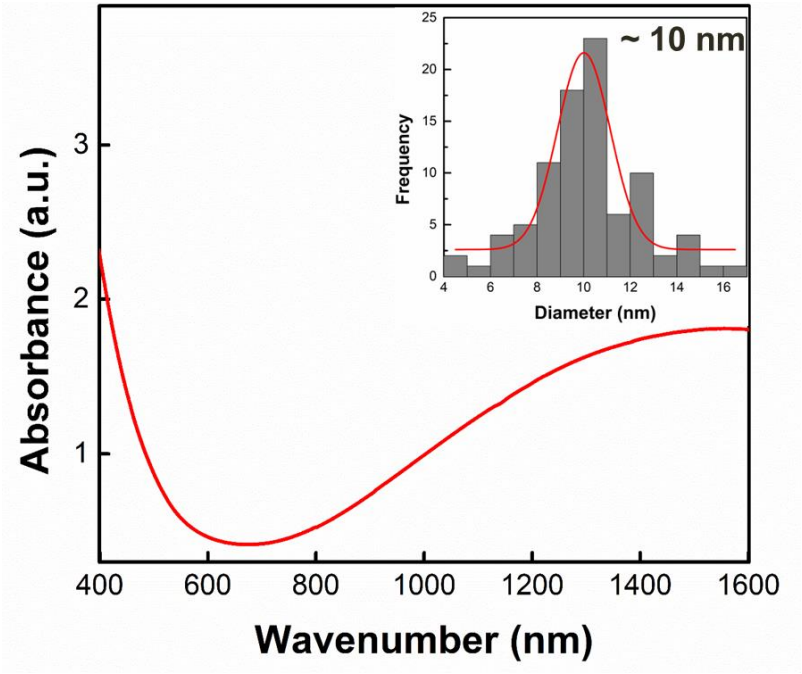

Fig. S2. UV-vis spectrum of TOA-Cu_xS NPs in toluene and the inset shows size distribution..

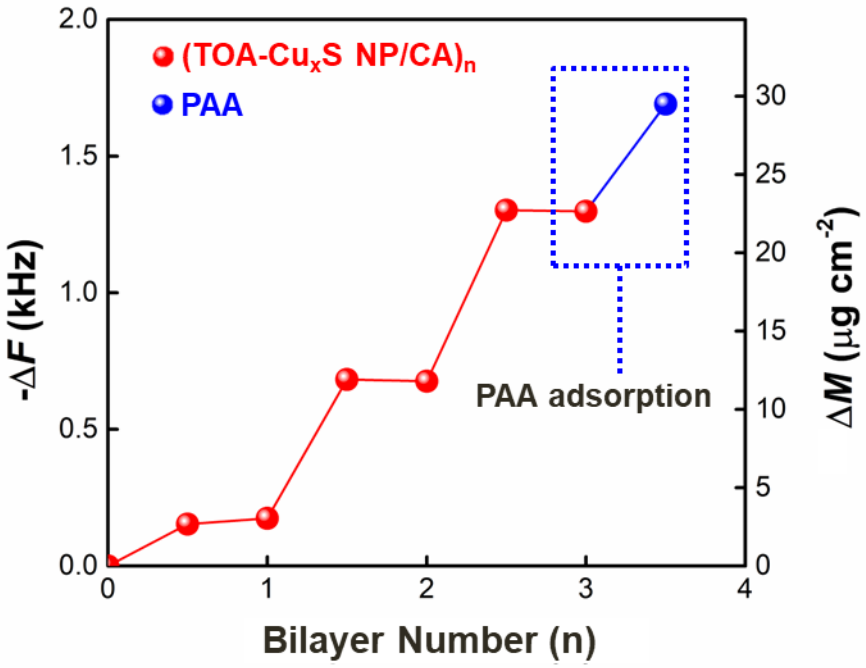

Fig. S3. QCM measurment data displaying the adsorption behaviour of PAA on outermost amine.

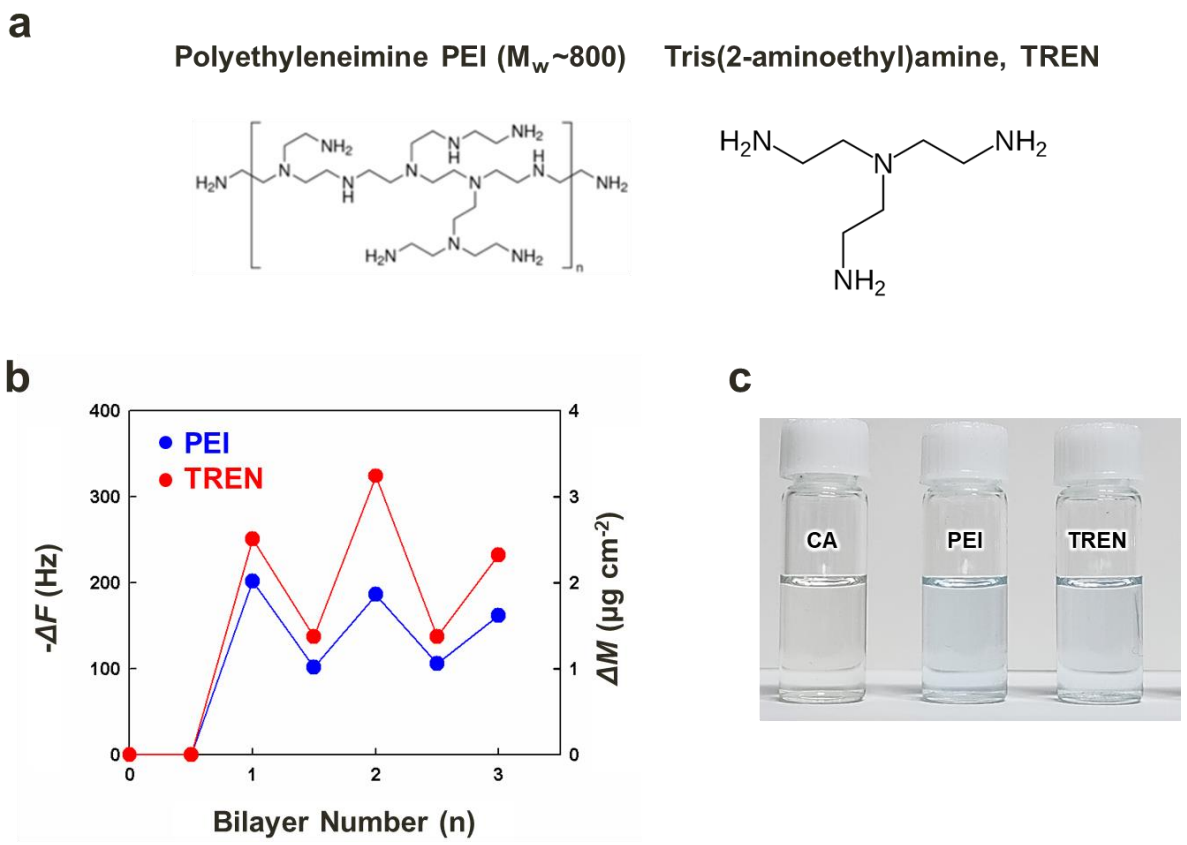

Fig. S4. (a) Chemical structures of amine-rich molecules, PEI and TREN. (b) The mass change of deposited materials on QCM electrode through LbL process between TOA-Cu_xS NP and amine-rich molecules. The result showed decrease in deposited mass after dipping process in amine-rich molecule solutions. (c) Digital images displaying dissolution of TOA-Cu_xS NPs in PEI and TREN solution. Slightly blue color of the amine-rich linker solution was observed after the LbL process, whereas the color of cysteamine solution remain unchanged.

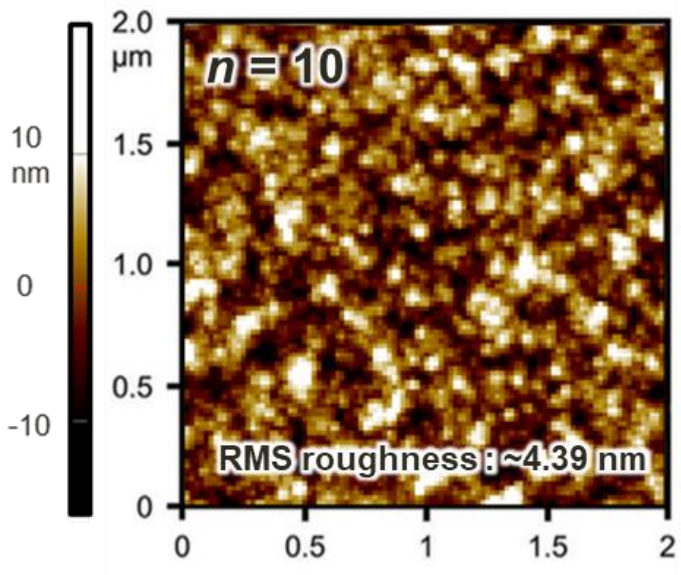

Fig. S5. AFM topographic images of (TOA-Cu_xS NP/CA)$_{10}$ multilayers deposited onto the silicon wafer substrate within a scan area of 2 μm × 2 μm.

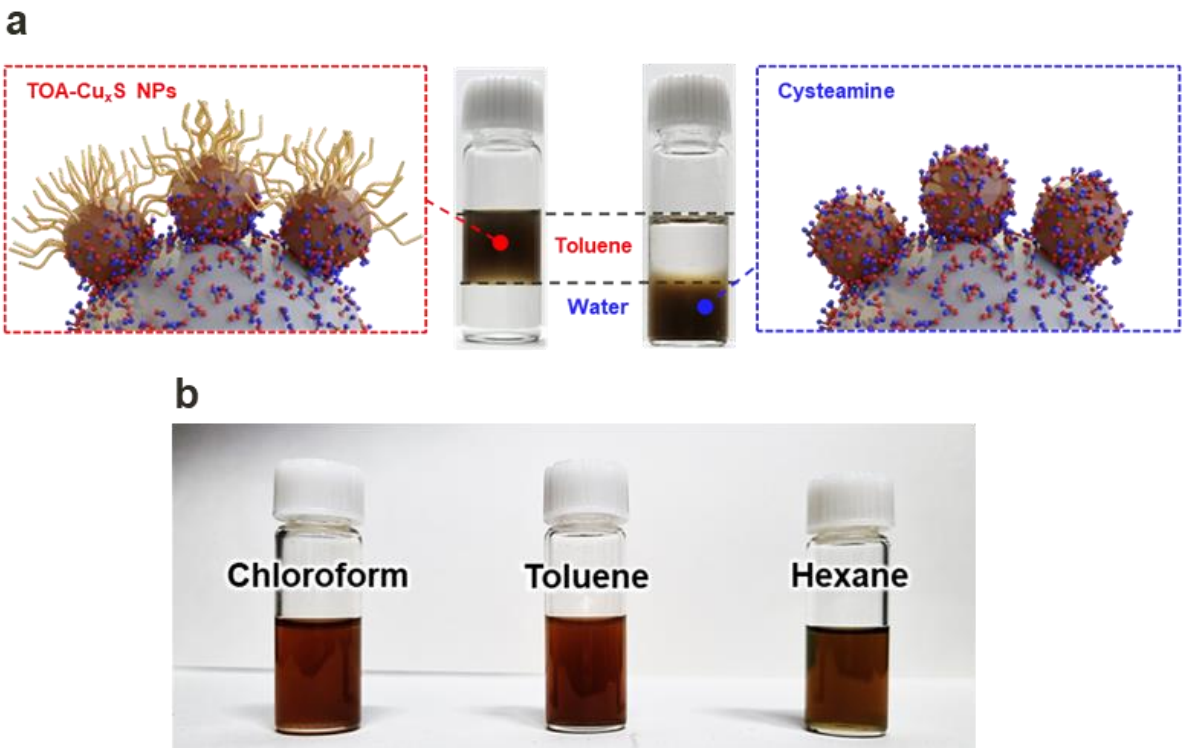

Fig. S6. (a) Schematic and photographic images displaying colloidal dispersion depending on the surface wettability of the outermost layer. (b) Photographic images showing dispersion stability of TOA-Cu_xS NP coated SiO_2 colloids in non-polar solvents, chloroform, tolu ene, and hexane.

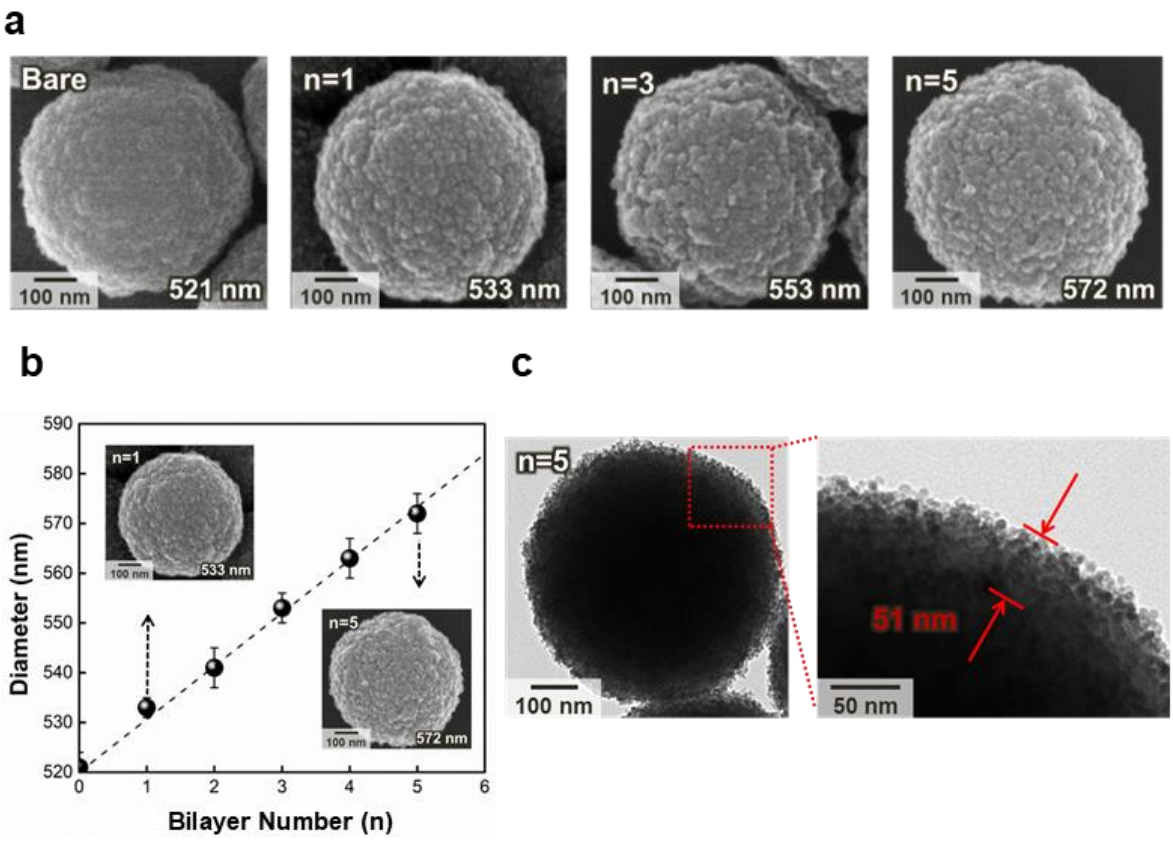

Fig. S7. (a) FE-SEM images of (TOA-Cu_xS NP/CA)$_n$ multilayers-coated SiO_2 colloids with bare, n = 1, 3, and 5. (b) Size change of (TOA-Cu_xS NP/CA)$_n$ multilayers-coated SiO_2 colloids with increasing bilayer number (n) measured from the cross-sectional FE-SEM images (inset). (c) HR-TEM images of (TOA-Cu_xS NP/CA)$_5$ multilayers-coated SiO_2 colloids at different magnifications.

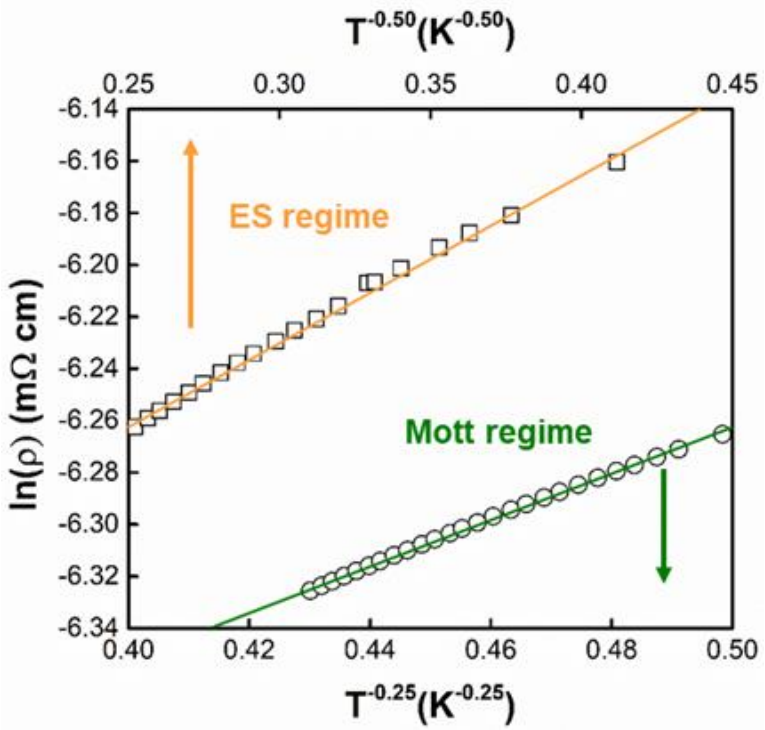

Fig. S8. Conduction mechansim of (TOA-Cu_xS NP/CA)$_{10}$ multilayer in the low temperature range (> 30K). In the temperature range of 29 to 16 K, Mott-VRH (plot of ln(ρ) vs. $T^{-1/4}$) was dominant conduction mechanism following the equation :

$$\rho(T) = \rho_M \, exp\left[\left(\frac{T_M}{T}\right)^{\frac{1}{1+n}}\right] \quad (1)$$

where ρ_M, T_M, and n refers to a constant, Mott's characteristic temrperature, and dimensionality, respectively. ES-VRH conduction mechanism was observed in the temperature range of 16 to 5 K showing a linear dependence in ln(ρ) vs. $T^{-1/2}$. The ES-VRH equation is given as :

$$\rho(T) = \rho_{ES} \, exp\left[\left(\frac{T_{ES}}{T}\right)^{\frac{3}{3+n}}\right] \quad (2)$$

where ρ_{ES}, T_{ES}, and n refers to a constant, ES characteristic temrperature, and dimensionality, respectively.

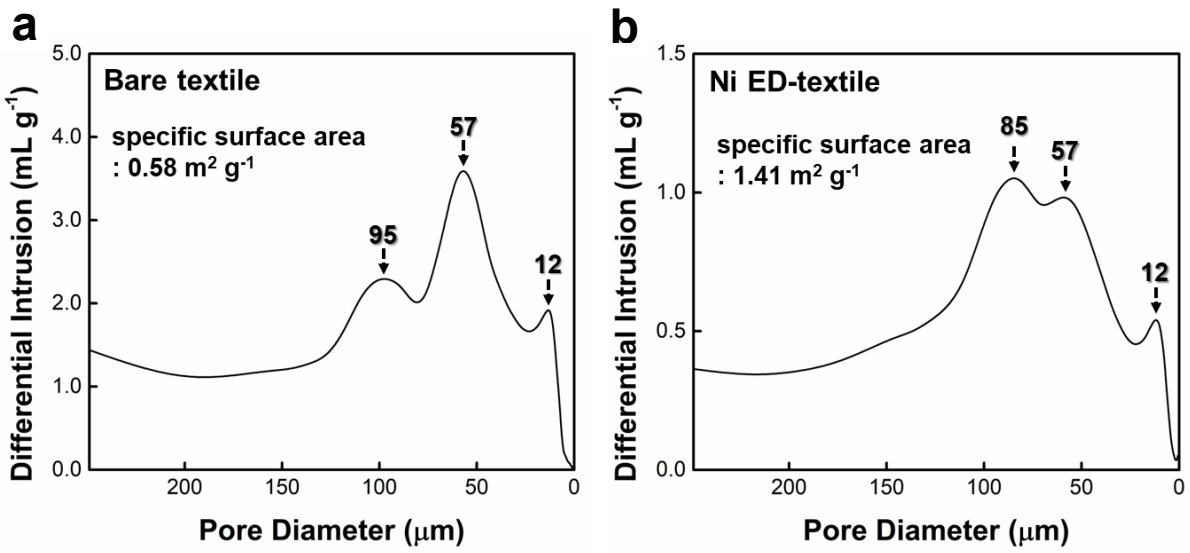

Fig. S9. Mercury intrusion data. Differential intrusion volume of mercury versus pore diameter for (a) bare cotton, and (b) Ni ED–textile using mercury porosimetry technique. The pore size in the Ni ED–textile ranges from ~3 to ~120 μm, with three distinct peaks at 12, 57, and 85 μm, which are similar to the bare cotton (i.e., 12, 57, and 95 μm). This indicates that the pores on the Ni ED–textile slightly decreased with the formation of the Ni layer.

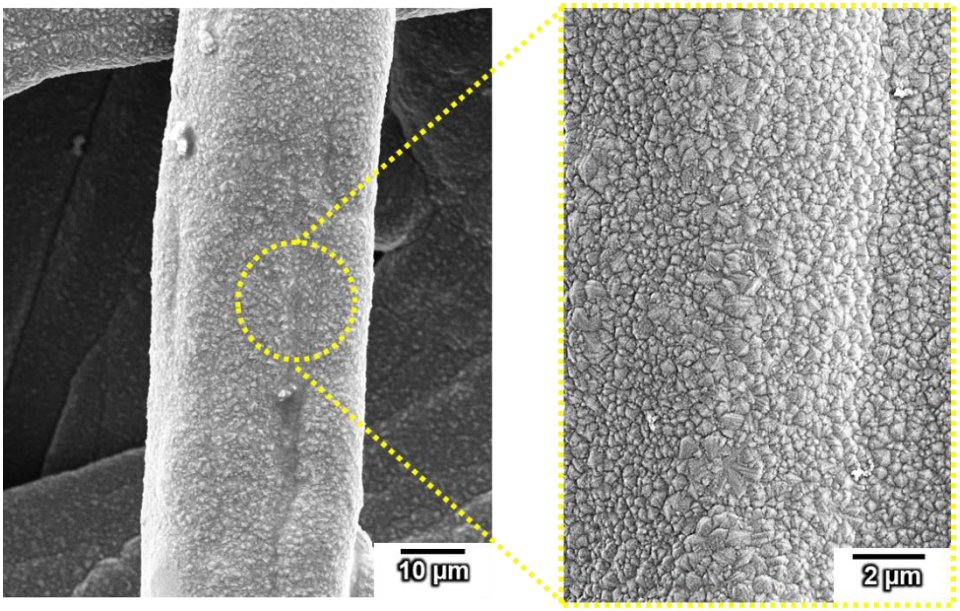

Fig. S10. FE-SEM image displaying Ni protuberances on fibril surface of Ni ED-textile.

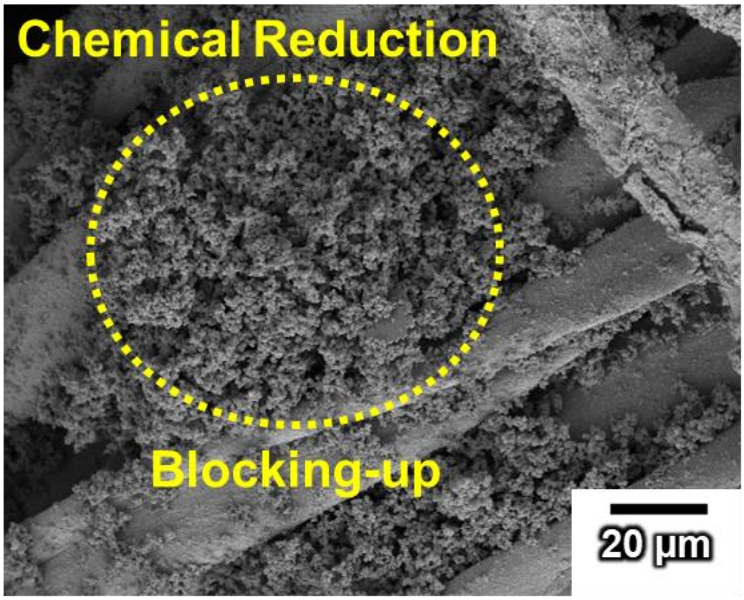

Fig. S11. FE-SEM images of Ni-textile using chemical reduction process. Non-conformal coating with partially aggregated Ni metal was observed.

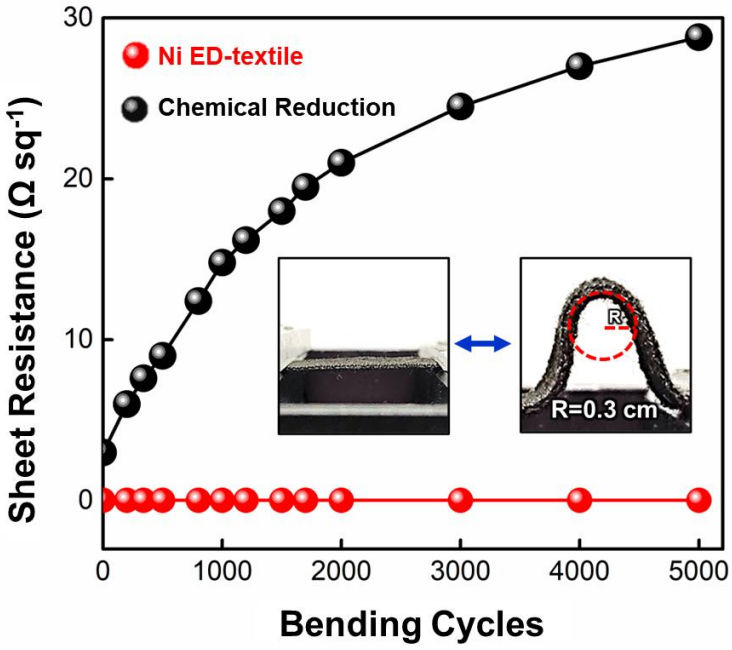

Fig. S12. Sheet resistance of ED Ni-textile and chemically reduced textile as a function of the bending cycles.

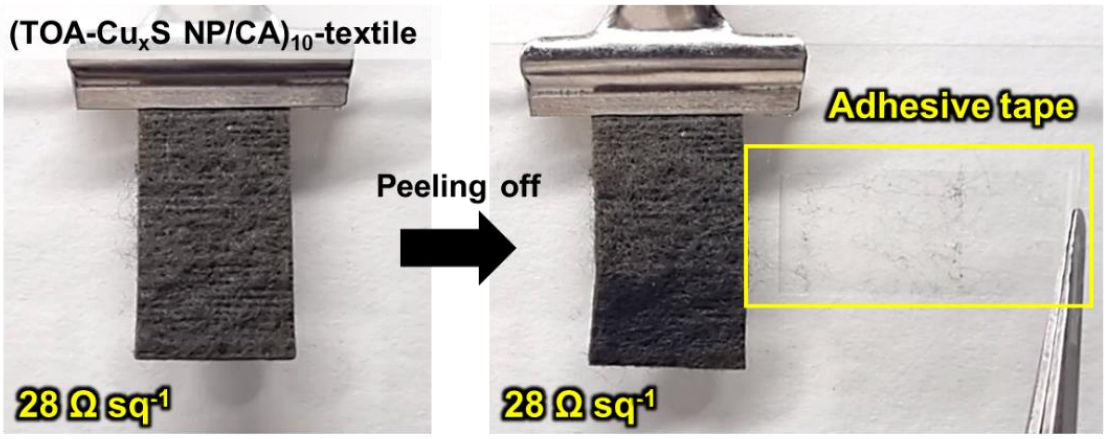

Fig. S13. Adhesion test of (TOA-Cu_xS NP/CA)$_{10}$-textile with 3M adhesive tape (from 3M Science Corp.). The yellow box indicates the tape surface after peeling off the tape from the (TOA-Cu_xS NP/CA)$_{10}$-textile.

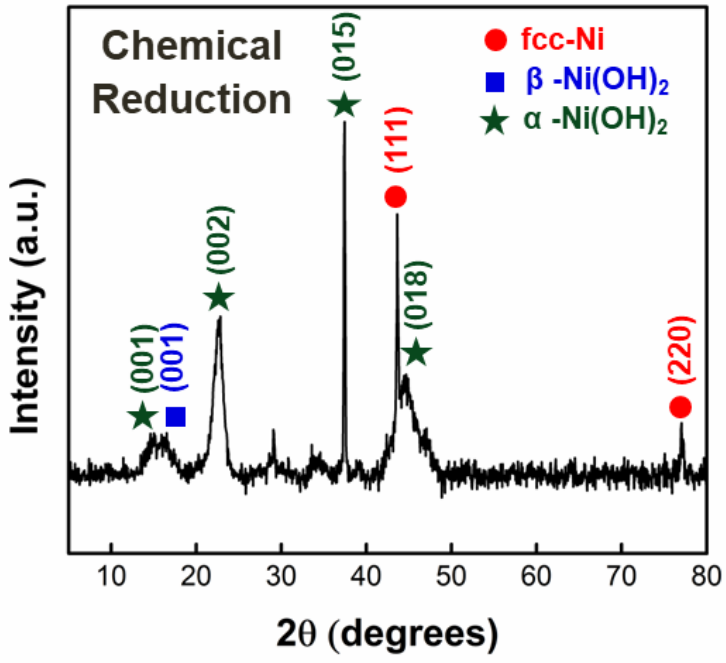

Fig. S14. XRD spectra of the chemically reduced Ni-textile.

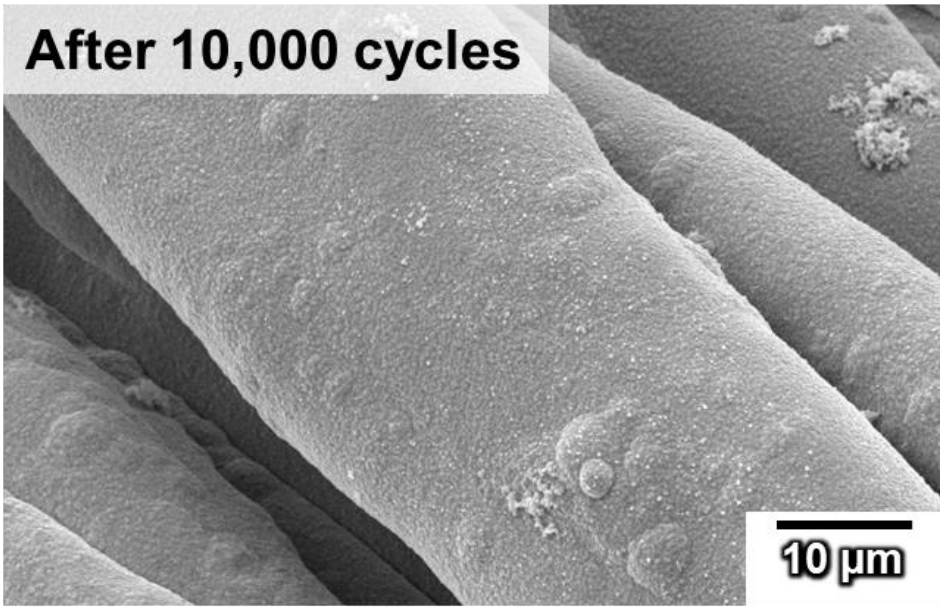

Fig. S15. FE-SEM images of Ni ED-textile after 10,000 cycles of electrochemical test.

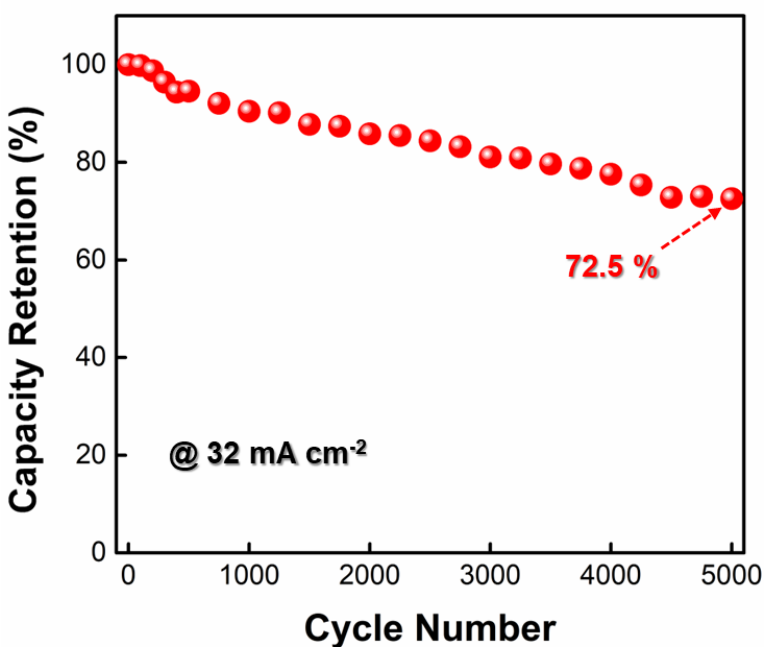

Fig. S16. Capacitance retention of Ni ED-textile after 5,000 cycles of GCD measurement at a current density of 32 mA cm^{-2}

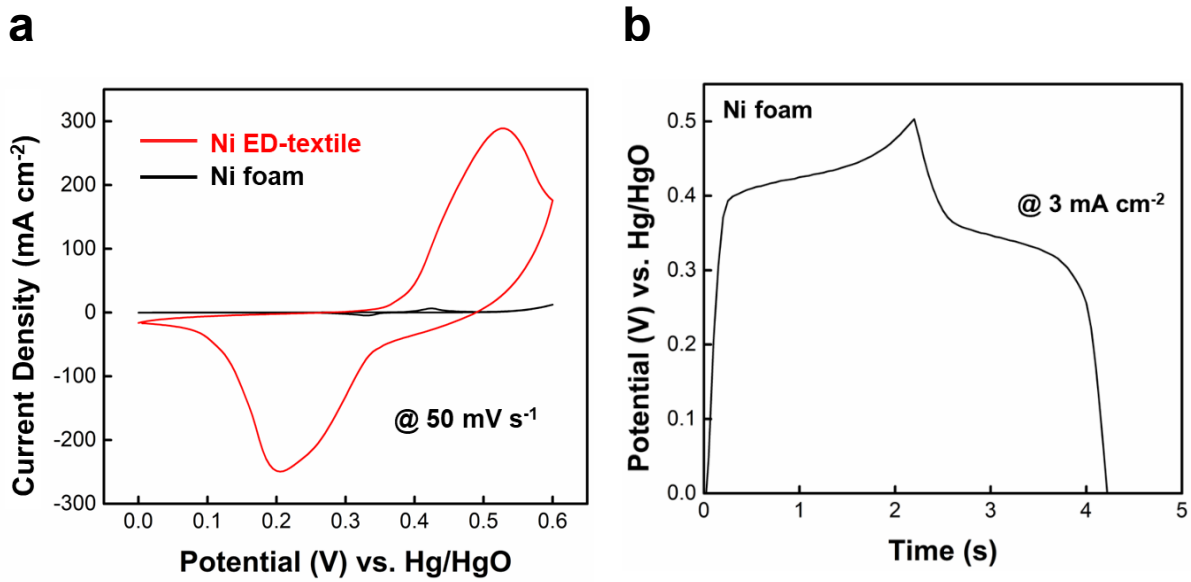

Fig. S17. (a) Comparison of CV curves (at scan rate of 50 mV s^{-1}) between Ni ED-textile and commercial Ni foam. (b) GCD profile of Ni foam measured at a current density of 3 mA cm^{-2}

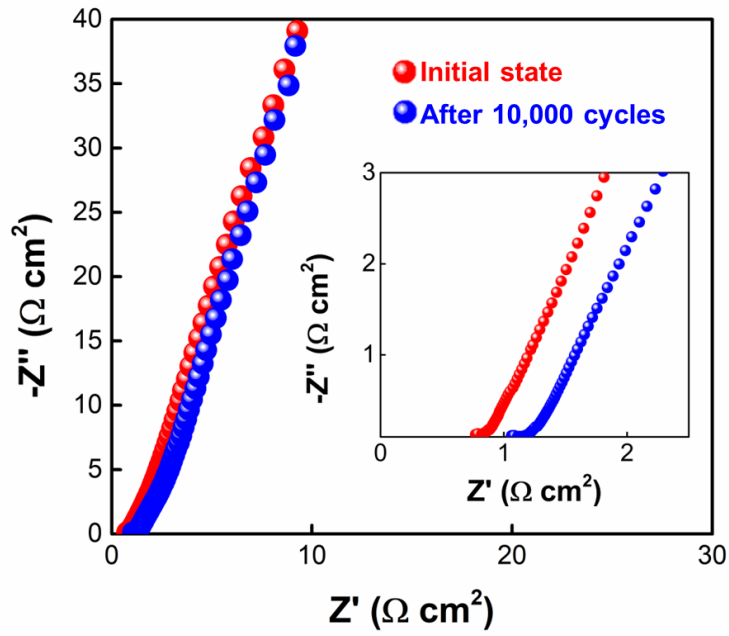

Fig. S18. Nyquist plots of ED Ni-textile electrodes over the frequency range from 10^5 to 0.1 Hz, measured at 0.1 V (amplitude potential ~5 mV) before and after 10,000 cycles of electrochemical stability test. The inset showed the Nyquist plots in the high frequency region.

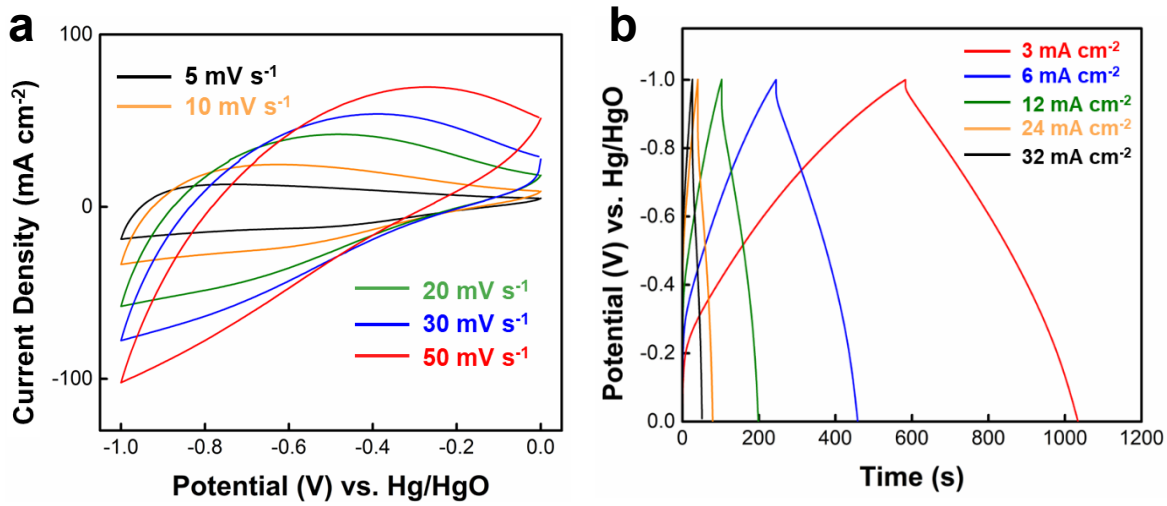

Fig. S19. (a) CV and (b) GCD curves of CT electrodes at various scan rates and current densities in three-electrode system.

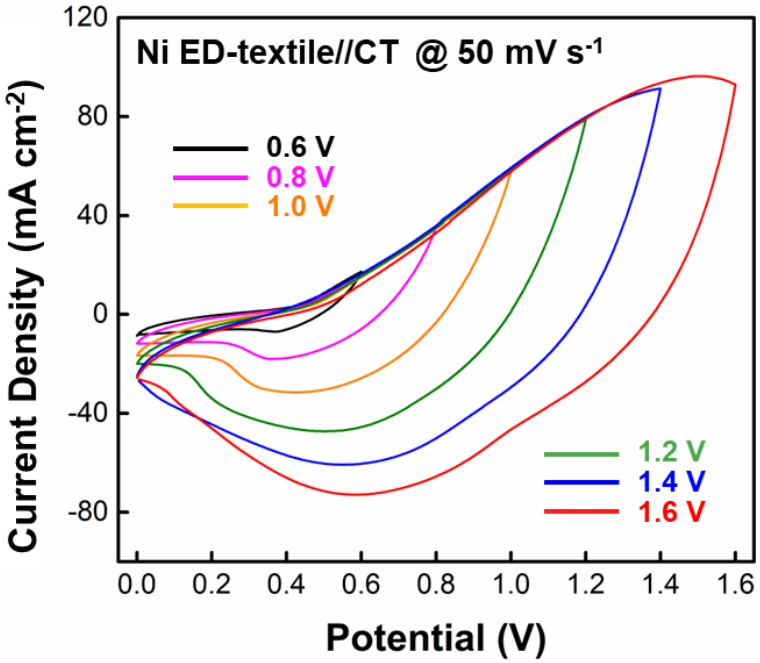

Fig. S20. CV curves of full-cell electrode measured at different potential window from 0.6 to 1.6 V.

Table S1. Performance comparison of textile-based supercapacitor electrodes.

Active Materials (Mass loading)	Substrate	Areal Capacitance	Specific Capacitance	Ref.
Ni ED-textile ($3.54\ mg\ cm^{-2}$)	Cotton textile	$2.56\ F\ cm^{-2}$ (@ $3\ mA\ cm^{-2}$)	$723\ F\ g^{-1}$ (@ $3\ mA\ cm^{-2}$)	**This work**
NiCo-LDH /Nanosheets ($0.87\ mg\ cm^{-2}$)	Polyester	$1.1\ F\ cm^{-2}$ (@ $3\ mA\ cm^{-2}$)	$648\ F\ g^{-1}$ (@ $1.69\ A\ g^{-1}$)	S1
$Co(OH)_2$ /MoCoS (-)	Carbon cloth	$1.5\ F\ cm^{-2}$ (@ $20\ mA\ cm^{-2}$)	$1711\ F\ g^{-1}$ (@ $22.20\ A\ g^{-1}$)	S2
V_2O_5/RGO ($2.3\ mg\ cm^{-2}$)	Graphite paper	$382.2\ mF\ cm^{-2}$	$178.5\ F\ g^{-1}$ (@ $0.05\ A\ g^{-1}$)	S3
RGO ($3.6\ mg\ cm^{-2}$)	Filter paper	$234\ mF\ cm^{-2}$	$67\ F\ g^{-1}$ (@ $0.05\ A\ g^{-1}$)	S4
W_2N/P ($1.2\ mg\ cm^{-2}$)	Carbon cloth	$765\ mF\ cm^{-2}$	$478\ F\ g^{-1}$ (@ $2\ mA\ cm^{-2}$)	S5
3D-graphene ($0.07\ mg\ cm^{-2}$)	Graphite paper	$15.6\ mF\ cm^{-2}$	$260\ F\ g^{-1}$ (@ $5\ mV\ s^{-1}$)	S6
MnO_2 ($16.8\ mg\ cm^{-2}$)	Carbon cloth	$3.0\ F\ cm^{-2}$ (@ $3\ mA\ cm^{-2}$)	$304\ F\ g^{-1}$ (@ $3\ A\ g^{-1}$)	S7
$ZnCo_2O_4$ ($0.896\ mg\ cm^{-2}$)	Carbon cloth	$2.3\ F\ cm^{-2}$ (@ $0.5\ mA\ cm^{-2}$)	$2034\ F\ g^{-1}$ (@ $0.45A\ g^{-1}$)	S8
Ppy ($0.96\ mg\ cm^{-2}$)	Carbon cloth	$136.9\ mF\ cm^{-2}$	$114\ F\ g^{-1}$ (@ $1\ mA\ cm^{-2}$)	S9
Bi_2O_3 ($9\ mg\ cm^{-2}$)	Carbon nanofiber paper	$545\ mF\ cm^{-2}$	$54\ F\ g^{-1}$ (@ $3\ mA\ cm^{-2}$)	S10
N-Fe_2O_3 ($4.3\ mg\ cm^{-2}$)	Carbon cloth	$277.3\ mF\ cm^{-2}$	$64.5\ F\ g^{-1}$ (@ $10\ mV\ S^{-1}$)	S11
PANI ($0.68\ mg\ cm^{-2}$)	SWCNT paper	$330\ mF\ cm^{-2}$	$533.3\ F\ g^{-1}$ (@ $0.2\ mA\ cm^{-2}$)	S12
MWCNT-Mxene (-)	Carbon cloth	$114.58\ mF\ cm^{-2}$	$71.61\ F\ g^{-1}$ (@ $5\ mV\ S^{-1}$)	S13
PEDOT/VN ($2.0\ mg\ cm^{-2}$)	Carbon cloth	$452.4\ mF\ cm^{-2}$	$226.2\ F\ g^{-1}$ (@ $1\ A\ g^{-1}$)	S14
PANI/CNT (-)	Polyester	$386\ mF\ cm^{-2}$	-	S15
Graphene ($5.5\ mg\ cm^{-2}$)	Cotton	$232\ mF\ cm^{-2}$	$42.2\ F\ g^{-1}$ (@ $1\ mA\ cm^{-2}$)	S16
Ppy ($5.7\ mg\ cm^{-2}$)	Cotton	$1325\ mF\ cm^{-2}$	$232.5\ F\ g^{-1}$ (@ $2\ mA\ cm^{-2}$)	S17
RGO/Ni-MOF ($4.04\ mg\ cm^{-2}$)	Polyester	$260\ mF\ cm^{-2}$	$64.3\ F\ g^{-1}$ (@ $4\ mA\ cm^{-2}$)	S18
PANI/rGO (-)	Polyester	$1.2\ F\ cm^{-2}$ (@ $1\ mA\ cm^{-2}$)	$389\ F\ g^{-1}$ (@ $0.32\ A\ g^{-1}$)	S19
NiCo-LDH ($0.03\ mg\ cm^{-2}$)	PET fiber	$0.6\ F\ cm^{-2}$ (@ $0.6\ mA\ cm^{-2}$)	$2105\ F\ g^{-1}$ (@ $2\ A\ g^{-1}$)	S20

References

[S1] G. Nagaraju, S. C. Sekhar, L. K. Bharat, J. S. Yu, Wearable fabrics with self-branched bimetallic layered double hydroxide coaxial nanostructures for hybrid supercapacitors, ACS Nano 11 (2017) 10860.

[S2] S. J. Patil, D. Lee, Scalable and ascendant synthesis of carbon cloth coated hierarchical core–shell CoMoS@$Co(OH)_2$ for flexible and high-performance supercapacitors, J. Mater. Chem. A 6 (2018) 9592.

[S3] C. Y. Foo, A. Sumboja, D. J. Hong Tan, J. Wang, P. S. Lee, Flexible and highly scalable V_2O_5-rGO electrodes in an organic electrolyte for supercapacitor devices, Adv. Energy Mater. 4 (2014) 1400236.

[S4] A. Sumboja, C. Y. Foo, X. Wang, P. S. Lee, Large areal mass, flexible and free-standing reduced graphene oxide/manganese dioxide paper for asymmetric supercapacitor device, Adv. Mater. 25 (2013) 2809.

[S5] D. P. Dubal, N. R. Chodankar, S. Qiao, Tungsten nitride nanodots embedded phosphorous modified carbon fabric as flexible and robust electrode for asymmetric pseudocapacitor, Small 15 (2019) 1804104.

[S6] A. Ramadossc, K.-Y. Yoon, M.-J. Kwak, S.-I. Kim, S.-T. Ryu, J.-H. Jang, Fully flexible, lightweight, high performance all-solid-state supercapacitor based on 3-Dimensional-graphene/graphite-paper, J. Power Sources, 337 (2017) 159.

[S7] Z. Huang, Y. Song, D. Feng, Z. Sun, X. Sun, X. Liu, High mass loading MnO_2 with hierarchical nanostructures for supercapacitors, ACS Nano 12 (2018) 3557.

[S8] D. Kong, Y. Wang, S. Huang, J. Hu, Y. V. Lim, B. Liu, S. Fan, Y. Shi, H. Y. Yang, 3D self-branched zinc-cobalt Oxide@ N-doped carbon hollow nanowall arrays for high-performance asymmetric supercapacitors and oxygen electrocatalysis, Energy Storage Mater. 23 (2019) 653.

[S9] T. Liu, L. Finn, M. Yu, H. Wang, T. Zhai, X. Lu, Y. Tong, Y. Li, Polyaniline and polypyrrole pseudocapacitor electrodes with excellent cycling stability, Nano Lett. 14 (2014) 2522.

[S10] H. Xu, X. Hu, H. Yang, Y. Sun, C. Hu, Y. Huang, Flexible asymmetric micro-supercapacitors based on Bi_2O_3 and MnO_2 nanoflowers: larger areal mass promises higher energy density, Adv. Energy Mater. 5 (2015) 1401882.

[S11] X. Lu, Y. Zeng, M. Yu, T. Zhai, C. Liang, S. Xie, Muhammad-Sadeeq Balogun, Yexiang Tong Oxygen-deficient hematite nanorods as high-performance and novel negative electrodes for flexible asymmetric supercapacitors, Adv. Mater. 26 (2014) 3148.

[S12] D. Ge, L. Yang, L. Fan, C. Zhang, X. Xiao, Y. Gogotsi, S. Yang, Foldable supercapacitors from triple networks of macroporous cellulose fibers, single-walled carbon nanotubes and polyaniline nanoribbons, Nano Energy 11 (2015) 568.

[S13] H. Li, R. Chen, M. Ali, H. Lee, M. J. Ko, In situ grown MWCNTs/MXenes nanocomposites on carbon cloth for high-performance flexible supercapacitors, Adv. Funct. Mater. 30 (2020) 2002739.

[S14] M. Chen, H. Fan, Y. Zhang, X. Liang, Q. Chen, X. Xia, Coupling PEDOT on mesoporous vanadium nitride arrays for advanced flexible all-solid-state supercapacitors, Small 16 (2020) 2003434.

[S15] F. C. R. Ramirez, P. Ramakrishnan, Z. P. Flores-Payag, S. Shanmugam, C. A. Binag, Polyaniline and carbon nanotube coated pineapple-polyester blended fabric composites as electrodes for supercapacitors, Synth. Met. 230 (2017) 65.

[S16] X. He, P. Song, X. Shen, Y. Sun, Z. Ji, H. Zhou, B. Li, Chitosan-assisted synthesis of wearable textile electrodes for high-performance electrochemical energy storage, Cellulose 26 (2019) 9349.

[S17] Y. Lianga, W. Weng, J. Yanga, L. Liu, Y. Zhang, L. Yang, X. Luo, Y. Cheng, M. Zhu, Asymmetric fabric supercapacitor with a high areal energy density and excellent flexibility, RSC Adv. 7 (2017) 48934.

[S18] C. Cheng, J. Xu, W. Gao, S. Jiang, R. Guo, Preparation of flexible supercapacitor with RGO/Ni-MOF film on Ni-coated polyester fabric, Electrochim. Acta, 318 (2019) 23.

[S19] X. Li, L. Yuan, R. Liu, H. He, J. Hao, Y. Lu, Y. Wang, G. Liang, G. Yuan, Z. Guo, Engineering textile electrode and bacterial cellulose nanofiber reinforced hydrogel

electrolyte to enable high-performance flexible all-solid-state supercapacitors, Adv. Energy Mater. 11 (2021) 2003010.

[S20] G. Nagaraju, G. S. R. Raju, Y. H. Ko, J. S. Yu, Hierarchical Ni–Co layered double hydroxide nanosheets entrapped on conductive textile fibers: a cost-effective and flexible electrode for high-performance pseudocapacitors, Nanoscale 8 (2016) 812.